Illumination conditions of the lunar polar regions using LOLA topography

E. Mazarico [a,b,*,1], G.A. Neumann [a], D.E. Smith [a,b], M.T. Zuber [b], M.H. Torrence [a,c]

[a] NASA Goddard Space Flight Center, Planetary Geodynamics Laboratory, Greenbelt, MD 20771, United States
[b] Massachusetts Institute of Technology, Department of Earth, Atmospheric and Planetary Sciences, Cambridge, MA 02139, United States
[c] Stinger Ghaffarian Technologies, Inc., Greenbelt, MD 20770, United States

A B S T R A C T

We use high-resolution altimetry data obtained by the Lunar Orbiter Laser Altimeter instrument onboard the Lunar Reconnaissance Orbiter to characterize present illumination conditions in the polar regions of the Moon. Compared to previous studies, both the spatial and temporal extent of the simulations are increased significantly, as well as the coverage (fill ratio) of the topographic maps used, thanks to the 28 Hz firing rate of the five-beam instrument. We determine the horizon elevation in a number of directions based on 240 m-resolution polar digital elevation models reaching down to ~75° latitude. The illumination of both polar regions extending to ~80° can be calculated for any geometry from those horizon longitudinal profiles. We validated our modeling with recent Lunar Reconnaissance Orbiter Wide-Angle Camera images. We assessed the extent of permanently shadowed regions (PSRs, defined as areas that never receive direct solar illumination), and obtained total areas generally larger than previous studies (12,866 and 16,055 km^2, in the north and south respectively). We extended our direct illumination model to account for singly-scattered light, and found that every PSR does receive some amount of scattered light during the year. We conducted simulations over long periods (several 18.6-years lunar precession cycles) with a high temporal resolution (6 h), and identified the most illuminated locations in the vicinity of both poles. Because of the importance of those sites for exploration and engineering considerations, we characterized their illumination more precisely over the near future. Every year, a location near the Shackleton crater rim in the south polar region is sunlit continuously for 240 days, and its longest continuous period in total darkness is about 1.5 days. For some locations small height gains (~10 m) can dramatically improve their average illumination and reduce the night duration, rendering some of those particularly attractive energy-wise as possible sites for near-continuous sources of solar power.

© 2010 Elsevier Inc. All rights reserved.

1. Introduction

1.1. Rationale

The Lunar Reconnaissance Orbiter (LRO) (Chin et al., 2007; Tooley et al., 2010) is a NASA mission from the Exploration Systems Mission Directorate. Launched on June 18th, 2009, the spacecraft entered lunar orbit a few days later, and after an extended commissioning phase, achieved its ~50-km-altitude polar mapping orbit on September, 15th, 2009. One of the measurement objectives of the LRO mission is the characterization of the illumination environment of the Moon's polar regions at relevant temporal scales. The Lunar Orbiter Laser Altimeter (LOLA) (Smith et al., 2010a) has enabled the collection of a high-resolution, geodetically-precise topography dataset that includes the highest resolution grids of polar topography to date (Smith et al., 2010b).

LOLA topography combined with a lunar ephemeris (Williams et al., 2008) can be used to characterize the illumination conditions at the lunar poles. Regions that never receive direct solar illumination (permanently shadowed regions, or PSRs) are of special scientific interest because their very cold temperatures (Paige et al., 2010) may sequester volatiles such as ice (Watson et al., 1961).

The present modeling effort was originally started to better understand, from an engineering standpoint, the thermal environment of the LOLA instrument due to the illumination reflected by the lunar surface. The model was also used in support of the Lunar Crater Observation and Sensing Satellite (LCROSS) mission (Colaprete et al., 2010), for the targeting of the LCROSS impact (on October 9th, 2009) and for ground telescope observation.

A better understanding of the illumination conditions in the lunar polar regions is also important to the planning of future lander missions, for traverse planning and also for power and thermal constraints informing engineering design (e.g., Fincannon, 2008).

* Corresponding author. Address: NASA GSFC, Code 698, B34 W271, Greenbelt, MD 20771, United States.
E-mail address: erwan.m.mazarico@nasa.gov (E. Mazarico).
[1] Present address: Massachusetts Institute of Technology, Department of Earth, Atmospheric and Planetary Sciences, Cambridge, MA 02139, United States.

1.2. Previous work

Due to the possible presence of volatiles near the poles of the Moon in PSRs (Watson et al., 1961), illumination near the lunar poles has long been a subject of interest. The poor knowledge of the relief near the poles prevented forward-simulations from topography models, and spacecraft imagery provided the earliest constraints on polar illumination (Arnold, 1979).

The Clementine spacecraft, in an elliptical orbit, provided additional imagery (Shoemaker et al., 1994; Bussey et al., 1999, 2005), but its laser altimeter could not obtain measurements at latitudes poleward of ~75° (Zuber et al., 1994; Smith et al., 1997). Consequently the first quantitative estimates of the topographic variance that produced the observed illumination patterns were based on extrapolation of the topographic power spectrum of equatorial and mid-latitude regions (Zuber and Smith, 1997). Bussey et al. (2003) also made simulations using simple crater shapes to estimate the amount of permanent shadow in the polar regions. Radar experiments performed with the Arecibo and Goldstone radio-telescopes acquired significantly improved south pole topography (Margot et al., 1999), which was used in later studies, such as Zuber and Garrick-Bethell (2005). However, the poor viewing geometry prevents farside polar topography from being observed, so illumination simulations cannot be reliably performed over a complete lunar month. Elevation models of the poles were constructed from Clementine image pairs (Cook et al., 2000; Archinal et al., 2006), adding farside coverage but lacking in resolution and precision (Bussey et al., 2003).

Noda et al. (2008) used data from the LALT instrument onboard the Japanese lunar mission SELENE (Araki et al., 2009) to perform illumination simulations. The improved quality of the LALT elevation model enabled a good agreement with previous Clementine imagery (Shoemaker et al., 1994), and PSRs and regions of maximum illumination were identified. However, the temporal extent of the simulation was significantly smaller than a complete lunar precession cycle (~18.6 years), and the results contained some artifacts due to orbital errors in the preliminary topography model used. Bussey et al. (2010) also used recent Kaguya topography to study the illumination conditions of the lunar south pole, with an emphasis on areas of maximum illumination.

1.3. Outline

In this work, we introduce an efficient framework for calculating the illumination conditions in the lunar polar regions, including scattered light. After comparing modeling results to recently acquired visible images, we present simulation results for both poles over long time periods. We characterize precisely PSRs and areas of maximum illumination, and we discuss the potential implications for volatile sequestration and lunar exploration.

2. Data and method

2.1. Data

The LOLA altimeter onboard LRO has been collecting data nearly continuously since it was commissioned on July 13th, 2009. LOLA is a high-rate multi-beam laser altimeter system (Smith et al., 2010a), which offers unprecedented resolution, especially in the along-track direction (~10 m at the 50 km mean altitude). The precision of the range measurements is ~10 cm, although the spacecraft radial position knowledge is currently less accurate.

We constructed digital elevation models (DEMs) of the polar regions, using a polar gnomonic projection on which great circle paths plot as straight lines. A resolution of 240 m was used as a compromise between sampling density, accuracy and computational cost. The LOLA altimetric points were geolocated based on the orbits produced by the LRO Navigation Team (Flight Dynamics Facility at GSFC). Topographic artifacts due to orbital errors (~10 m radially; <200 m in total position) are not very noticeable at the chosen grid spacing. The results presented below show that a resolution of 240 m is sufficient to reproduce actual lighting conditions accurately enough for long-timescale studies to be conducted.

Each region of interest extends from ~80° to the pole. Following Li et al. (2008), the calculations are based on a larger region (75–90°) to provide sufficient padding, and ensure the inclusion of all the possible topographic features that could occlude elements in the region of interest. In Fig. 1, we present the two polar DEMs created from the individual LOLA profiles. The north and south polar grids were formed with 48,382,470 and 91,698,177 altimetric measurements, respectively, from 2636 orbits between July 13th, 2009
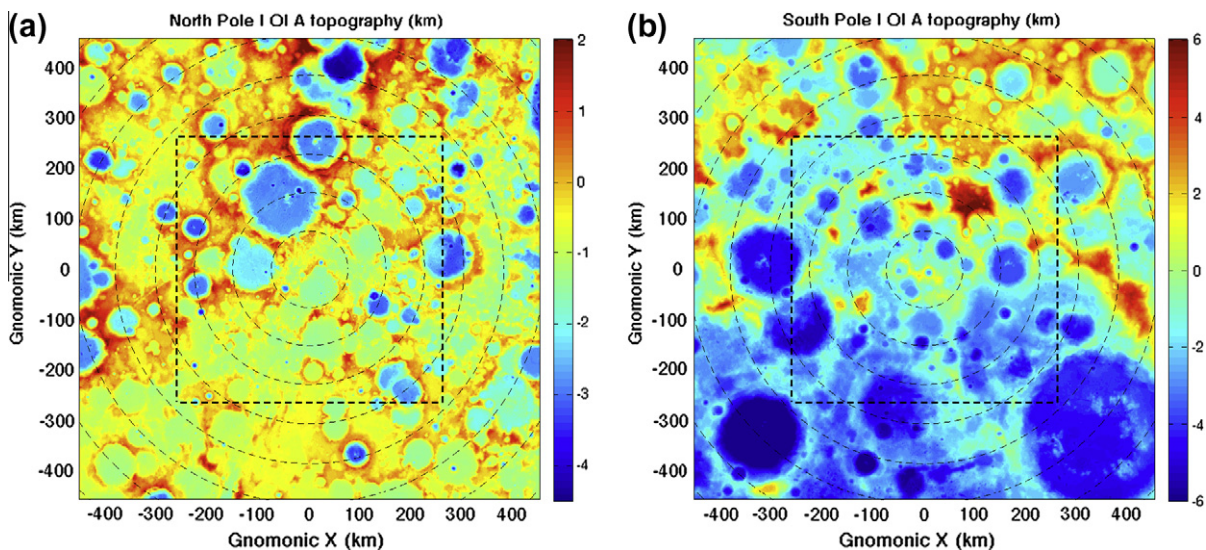
Fig. 1. North (a) and south (b) polar topographic models obtained from LOLA altimetry data collected to January 2010. The projection is polar gnomonic (true scale at the pole, with a reference radius of 1737.4 km), and the horizontal resolution is 240 m. The horizon elevations are only calculated for the subset region indicated by the dashed rectangle. Dashed circles indicate latitudes with a 2.5° separation. Note the different altitude scales (in kilometers).

and February 8th, 2010. The large difference in data quantity is due to the early commissioning phase (July–September 2009): the elliptical orbit, with its periapsis near the south pole, prevented data collection in the northern polar region. They have a spatial extent of 915 × 915 km, and contain 3812 × 3812 individual 240 × 240 m^2 grid elements (square pixels). Each region of interest (dashed rectangular outline) is 528 × 528 km and contains 2200 × 2200 elements. As stated above, the along-track resolution (related to the measurement frequency) is better than the cross-track resolution (related to the number of orbits); with 2636 tracks, the average longitudinal spacings at 80°, 85° and 88° are ∼720, ∼360 and ∼140 m, respectively. Compared to the Kaguya/LALT altimetric data used in recent studies (Noda et al., 2008; Bussey et al., 2010), the coverage is significantly improved thanks to the high firing frequency of the LOLA laser (28 Hz, with five beams, compared to 1 Hz, single-beam). The average fill ratio of the two polar maps increases from 6.7% and 5.6% in the north and south, respectively, to 33.3% and 37.2% with the LOLA maps used in this work. As LOLA measurements accumulate, these map fill ratios continue to improve. The maps released to the NASA Planetary Data System in September 2010 have fill ratio of ∼54.6% and ∼55.6% for those north and south polar regions, respectively.

2.2. Direct illumination: the horizon method

We use the horizon method to calculate the illumination condition of each surface element, a technique rarely used in past studies of the lunar poles. Previous investigators generally preferred ray-tracing method (e.g., Noda et al., 2008). While accurate, that latter is not necessarily well-adapted to illumination studies, which need to survey and address long time periods, as these ray-tracing calculations have to be repeated at each time step. Otherwise, approximations have to be made, such as restricting the temporal domain explored, or creating artificial months, which can for instance simulate the worst or best cases of solar illumination. Garrick-Bethell et al. (2005) used the horizon method with a radar-derived DEM (Margot et al., 1999), but they limited their study to areas of maximum illumination. Our work incorporates a more accurate DEM, increases the computational precision, and significantly extends the spatial and temporal coverage.

The modeling is divided in two independent steps:

– calculate and store the elevation of the horizon in a number of set directions, for every point in the region of interest;
– interpolate those fixed-direction horizon elevations to a given Sun location, and calculate the ratio of the solar disc which is visible.

The first step is very expensive (more than the ray-tracing method), but once the database has been created, obtaining an illumination map at a given epoch is very fast.

2.2.1. Step 1: creating the horizon database (elevation maps)

The algorithm we adopted is conceptually simple, but also computationally expensive. In the case of the Earth, some earlier efforts attempted to optimize the horizon calculation of a large number of points belonging to a uniform DEM grid. In particular, Dozier et al. (1981) presented a trick: small round-off approximations in the location of the nodes were made to drastically reduce the algorithmic complexity, from $O(N^2)$ to $O(N \cdot N_{th})$, where N^2 is the number of grid elements and N_{th} is the number of azimuthal directions considered.

While very attractive, this shortcut could not be applied satisfactorily to the lunar poles. First, Dozier et al. (1981) were concerned with relatively small regions on Earth, where the curvature of the planet could be ignored. Because it is necessary in the case of (large) polar regions of the Moon, additional complexity had to be included, which reduced the algorithm efficiency. Secondly, the interpolation errors arising from the low number of directions we originally considered ($N_{th} = 36$) lead to visible artifacts. This needed to be mitigated by increasing N_{th}, further reducing the appeal of that method.

For these reasons, we performed the calculations without any special assumption or approximation, at a high angular resolution ($N_{th} = 720$, e.g. a spacing of 0.5°, comparable to the apparent Sun diameter). While the computational cost is significant, such calculations need to be done only once per DEM.

Another issue to consider is that in order to preserve the apparent Sun direction from each point the elevations have to be calculated along line-of-sight paths. While commonly used for displaying polar imagery and topography, the polar stereographic projection does not conserve direction (i.e., points on a straight line are not in line-of-sight). The polar gnomonic projection allows an easy derivation of the maximum (obstructing) elevation (defining the horizon), by simply drawing lines from the point of interest.

A further benefit of working in gnomonic space is that the horizon data can be stored in a meaningful manner, by creating elevation maps. Instead of ordering the N_{th} horizon values of each point sequentially, N_{th} maps containing the elevation of the horizon in a given direction, over the whole region, are output. In the case of the Moon (and Mercury), the sub-solar latitudes are always near the equator, which project to very large distances in gnomonic space. Consequently, the ray paths are very nearly parallel (for our selected region, with the sub-solar latitude closest to the pole, the maximum angle difference is ∼2 × 10^{-7} degrees), and one elevation map represents the elevation of the horizon in the direction of the Sun, from the perspective of every point, for the whole region at once.

Fig. 2 describes the computational process. We go through each point of the region of interest sequentially. We calculate the elevation of all the grid elements as seen from the current perspective (Fig. 2a). This map is then interpolated along N_{th} straight lines originating from the current point (Fig. 2b). The spacing of the interpolating nodes is optimized and increases radially, as farther horizon-blocking features tend to be larger in horizontal scale. In each azimuthal direction, we can easily find the maximum elevation and its distance (Fig. 2c), which can be used to reconstruct the full horizon (Fig. 2d) are then stored in elevation maps (Fig. 2e). Increasing N_{th} does not significantly slow down the computations, a reason why we chose $N_{th} = 720$.

Because the computations for each point are independent, we can parallelize the calculation by assigning subset regions to various processors. For every point in its assigned region, sequentially, each process writes an index number and N_{th} horizon elevation values to a temporary file. All the temporary files are then combined into N_{th} elevation maps.

2.2.2. Step 2: obtaining regional illumination maps

Once the elevation maps have been created, it is straightforward to obtain the illumination map for a given epoch: we simply need to compare one such map of the horizon elevation with a map of the elevation of the Sun, as illustrated in Fig. 3.

The angular direction of the Sun in the gnomonic projection space, θ_{Sun}, is calculated, and the two closest elevation maps ($\theta_{Sun} \in [\theta_i; \theta_{i+1}]$) are used to determine the illumination conditions for the exact Sun angle. A map of the elevation of the Sun from every point in the region is obtained in the Cartesian frame.

We then compare those two maps. If the Sun was considered a point source, a grid element would be in sunlight if its horizon
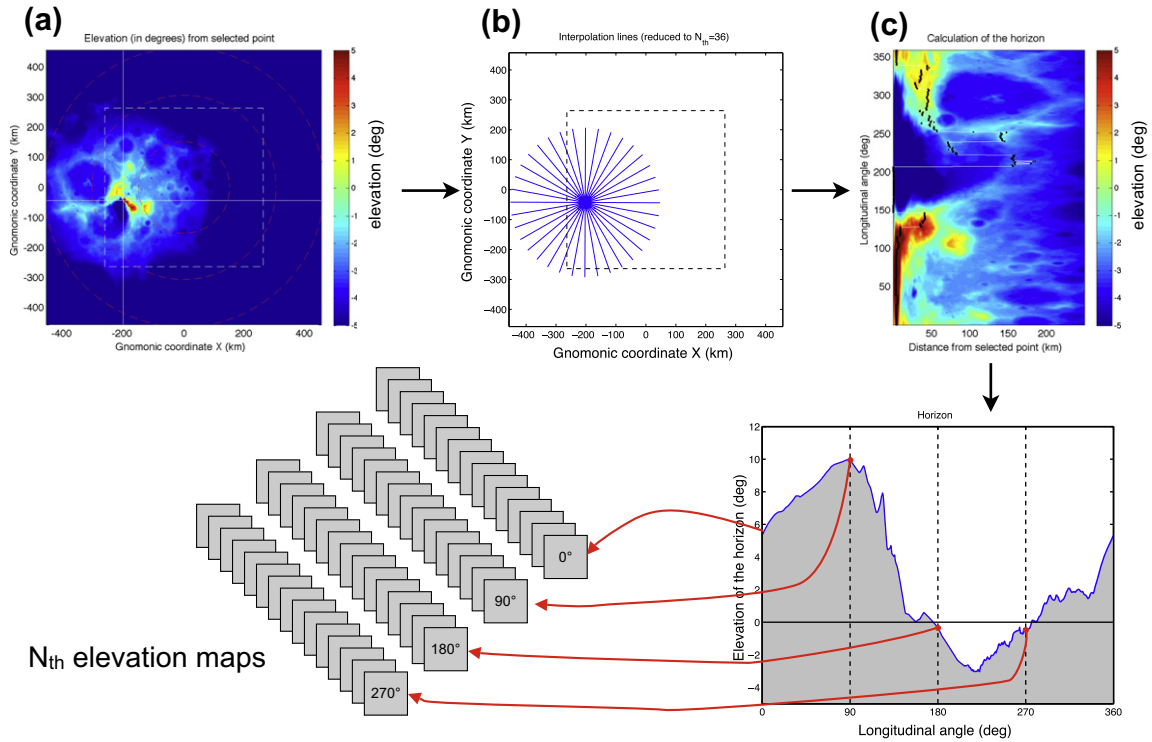
Fig. 2. For every point in the region of interest (dashed white line, a), we interpolate the calculated elevation of the whole map (a) onto a set of Nth segments (b). The distance and elevation of the horizon in each direction is obtained (c) (the black dot indicates the obstacle position). Each value of the full horizon (d) is then copied into the Nth elevation maps, at the location of the point considered (e).

elevation is lower than the Sun location. Instead, we model the Sun as an extended source, and calculate the ratio of the solar disc which is occulted by the horizon. The horizon is assumed to be a straight segment between the maps at θ_i and θ_{i+1} (which bound the Sun angular location).

The exact geometry of the Sun in the lunar frame is obtained from the DE421 ephemeris (Williams et al., 2008) and the lunar orientation model by Seidelmann et al. (2007). We use the SPICE toolkit (Acton, 1996). The position of the Sun and its angular radius (as an extended source) are updated at each time step.

As stated above, the appeal of the horizon method is that the computation of illumination maps is very fast. Averaged over 1000 time steps, each frame takes only about 0.7 s. It becomes possible to perform temporal simulations over very long time spans with reasonably small time steps.

In addition, the study of particular locations is greatly improved by having the full horizon in hand. We can interpolate the horizon elevations at the Sun angular directions over the chosen time period. Obtaining the illumination history of a point over any length of time and with any temporal resolution (e.g., Section 5) is then straightforward.

We use a similar approach to speed up long-duration calculations. We reorder the time steps by sorting the Sun angular directions, and perform all the time steps between θ_i and θ_{i+1} at once, reducing the overheads (file loading, etc.).

Three different maps can be output at every time step in the simulations: the Sun visibility (true if any part of the solar disc is visible), the Sun illumination (the percentage area of the Sun disc which is visible) and a proxy for the solar incident flux (which modulates the Sun illumination by the cosine of the incidence angle; the solar constant is not included). The incidence angle is calculated with respect to the normal vectors at the center of each square pixel, calculated from the neighboring pixels (centered-difference method).

2.3. Scattered illumination

Besides enabling a (nearly) exact survey of the PSR areas from a long-timescale calculations, the horizon method can be expanded to inform us, to first-order, on the potential implications of singly-scattered sunlight into PSRs. Regional multiple scattering, as modeled by ray-tracing methods (e.g., Vasavada et al., 1999), is beyond the scope of this study. We assess the (singly-) scattered light environment at discrete sites over long periods of time.

The flux scattered to a point O is given by:

$$F_o^{scattered}(t) = (1 - A_O) \sum_{P \in \mathcal{V}_O} A_P \mathcal{A}_P (F_\odot \sigma_P^\odot(t) \cos i_P^\odot(t)) \frac{\cos e_P \cos i_O}{d_{OP}^2}$$

$$\mathcal{L}_{OP} = (1 - A_O) \mathcal{A}_P A_P F_\odot \frac{\cos e_P \cos i_O}{d_{OP}^2}$$

$$\mathcal{A}_P = \frac{2\pi d_{OP}}{N_{th}} W_P$$

where $\mathcal{V}_O$ represents the set of points P which are visible from O.

Many terms in this equation are independent of the illumination conditions. Some are related to the topographic geometry between O and P: d_{OP} is the distance between O and P; A_P is the surface area of element P; e_P is the emission angle at P, i.e., the angle of the normal at P with respect to the line joining P and O; i_O is the incidence angle at O, i.e., the angle of the normal at O with that same OP line. Other constants are A_O and A_P, the surface albedo at O and P, and F_9, the solar flux. We define the scattering link between O and P, L_{OP}, which includes all those constants:

$$L_{OP} = (1 - A_O) A_P \frac{A_P F_9 \frac{\cos e_P \cos i_O}{d_{OP}^2}}{}$$

Time-dependent terms are i_P^9, the solar incidence angle at P, and V_P^9, the solar disc visibility ratio at P, as calculated in Section 2.2.
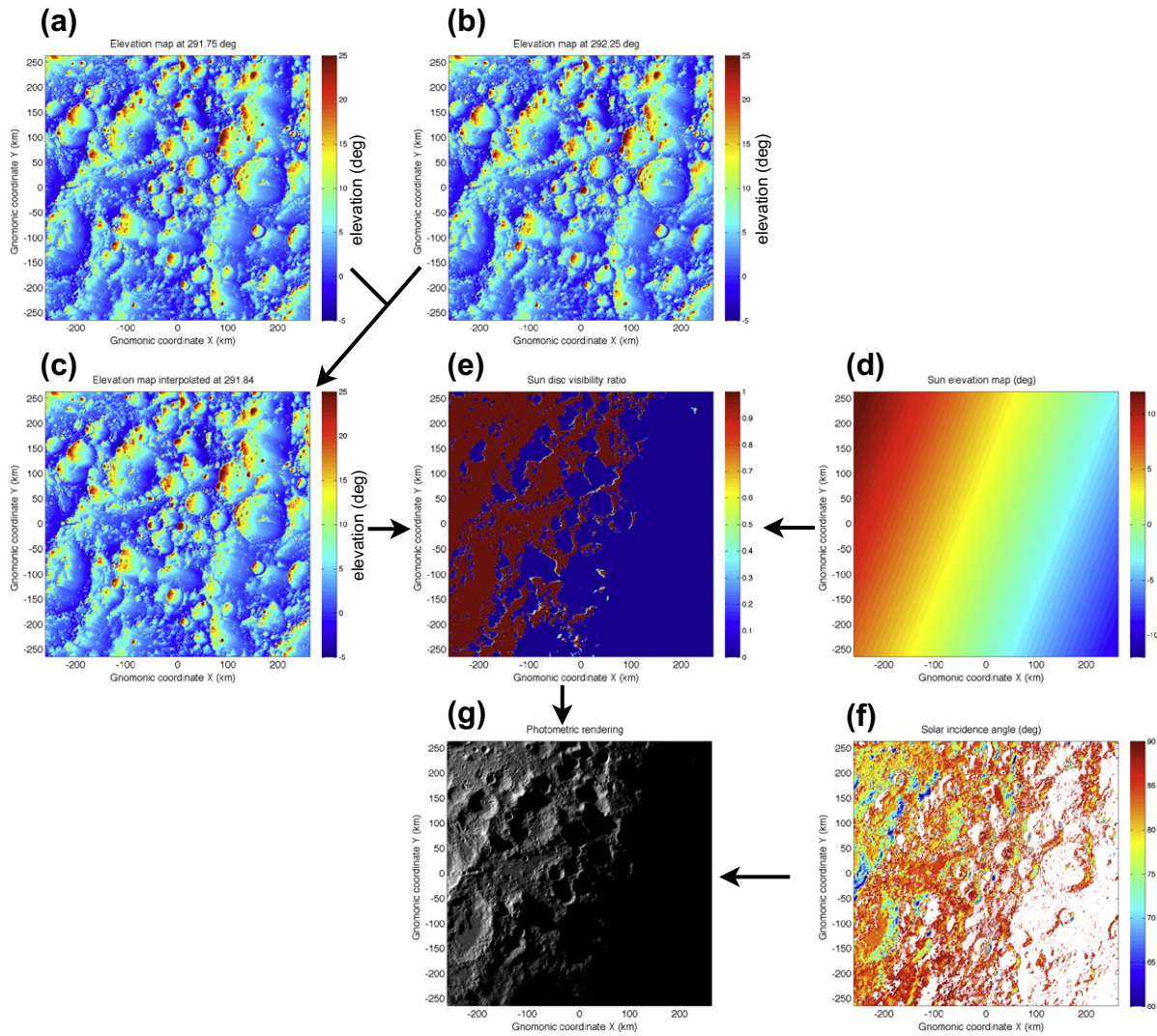
Fig. 3. The two appropriate (neighboring) elevation maps (a, b) are interpolated at the current sun direction (c). It is then combined with the calculated sun elevation map (d) to obtain a map of the sun visibility (e). For rendering purposes, a chosen photometric function uses a map of the incident angle of the sunrays (f) to obtain a photo-realistic view of the region (g).
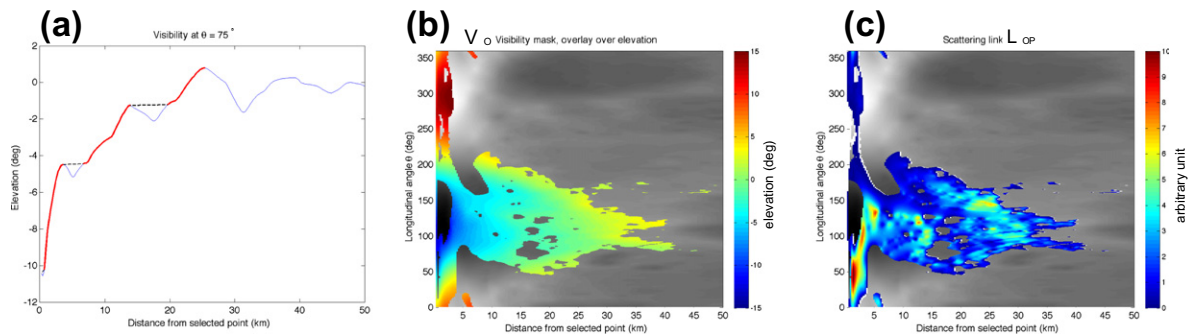
Fig. 4. (a) For each elevation profile (blue line; similar to those obtained in Fig. 2c), we step backwards from the maximum elevation (which defines the horizon) to select all the visible elements (thick red line); (b) a mask has been applied on the elevation (Fig. 2d), to display the non-visible elements in grayscale; (c) Same as (b), but instead of showing the elevation of the visible elements, we plot their "scattering link" with respect to the point of interest. (For interpretation of the references to colours in this figure legend, the reader is referred to the web version of this paper.)

For technical reasons, instead of considering the original DEM grid, we choose the P points along the N_{th} interpolation lines. The area of each sectorial ring is then defined by:

$$A_P = \frac{2rd_{OP}}{N_{th}} W_P$$

where W_P is its radial width (distance to the next P point radially).

We find V_O by stepping through the N_{th} elevation profiles (of Section 2.2.1). In each direction, we start from the horizon-defining element (the maximum elevation in the profile), and sweep inward, checking if any element closer to the target O than the point considered (P, the scatterer) has a larger elevation (Fig. 4a). The red segments indicate the elements which are visible from point O. We combine all the direction profiles, and obtain a "mask" of all the

elements *P* visible from *O* (see Fig. 4b, similar to Fig. 1c, but only the areas visible from *O* are in color). In that process, we also calculate the scattering link L_{OP} (Fig. 4c). For each point of interest *O*, we store the non-zero L_{OP} values (and the geographical locations of the corresponding *P* points).

In order to calculate the scattered flux received at *O* at a given time, we need to calculate the time-dependent parameters, and hence the illumination conditions of all the points with a non-zero scattering link. In practice, because we deal with a large number of points of interest, we calculate full-region illumination maps and apply to it all the scattering link masks. Section 4.2 demonstrates such an application.

3. General illumination results

3.1. Validation from imagery

It is important to validate illumination models with images taken by spacecraft, in order to confidently use the model over long time periods. The grazing sunlight on the polar relief (resulting from the low inclination of the Moon) produces large visual differences if the topography model used is incorrect.

Earlier studies used Clementine imagery for comparison, but the available topography (Zuber et al., 1994; Smith et al., 1997; Archinal et al., 2006) was not of sufficient quality to accurately reproduce the spacecraft images (Shoemaker et al., 1994). Bussey et al. (1999) and Bussey et al. (2005) combined Clementine images over several months to survey the best-illuminated regions in both polar regions. Several authors (e.g., Garrick-Bethell et al., 2005; Zuber and Garrick-Bethell, 2005 and Bryant, 2010) used a high-resolution radar-derived topography (Margot et al., 1999). However, large areas were not visible from the ground, especially on the farside, and slope/tilt ambiguities existed. Recently, Noda et al.

(2008) used a high-resolution topographic map obtained by the Kaguya laser altimeter (Araki et al., 2009) to study the illumination conditions at the lunar poles. Clementine imagery was used for comparison. Bussey et al. (2010) used a slightly more complete dataset from Kaguya LALT in their study, and showed in more detail the good match of their simulations with Clementine images.

We used polar images of the Lunar Reconnaissance Orbiter Camera (LROC) Wide-Angle Camera (WAC) onboard the LRO spacecraft (Robinson et al., 2010). Compared to Clementine images, these images are very extensive (>100 km-wide swaths) and frequent (once per orbit, ~2 h). We used 24 images distributed over one full month (J. Oberst and F. Scholten, personal communication). In order to create photo-realistic renditions, we used a fit of the Clementine photometric function (McEwen, 1996) by Gaskell et al. (2008). Incidence, emission and phase angles were calculated for each grid element. The surface normal vectors were obtained directly from the LOLA DEM (Smith et al., 2010b). Fig. 5 shows a comparison of the model output with three LROC WAC mosaics of the south pole region. The agreement is visually excellent, showing that: the resolution chosen for the topography model (240 m) is adequate; the topography model can be used to accurate predict the illumination in the lunar polar regions; we can use the horizon method with confidence. A quantitative assessment of the model-image match (such as a simple correlation number) is hindered by brightness discrepancies due to the photometric model we used, as well as surface variations in albedo, composition and material freshness (e.g., Eliason et al., 1999). The focus of this work is not to determine the properties of lunar soil at the poles, and the interested reader is referred to Fig. S1 (in Supplementary material), which provides dozens of additional image comparisons for each pole and over the whole solar longitude range. A comparison with the ray-tracing method (Stubbs et al., 2010) at selected times showed good agreement.
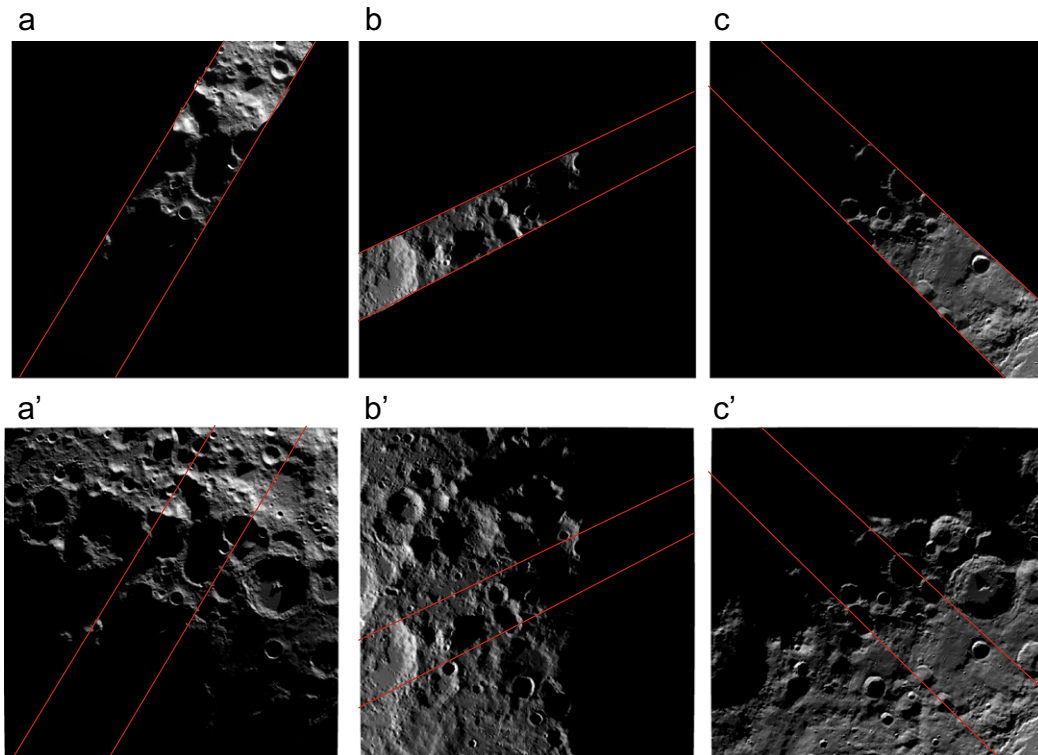
Fig. 5. (a, b, c) south pole LROC WAC images assembled by J. Oberst and F. Scholten (DLR) from orbits around the following UTC epochs: 2009-10-01 11:06; 2009-10-12 15:00; 2009-10-20 22:52. (a′, b′, c′) Corresponding model outputs. The viewpoint is from a radius of 3000km, above the south pole.

3.2. Validation of some assumptions

As described in Section 2.2.1, we use N_{th} = 720 azimuthal directions in the horizon elevation calculations. To further validate our model parameters, we calculated illumination maps with reduced azimuthal resolution. When we degrade it to 5° (instead of 0.5°), about 3% of the grid elements over the whole region of interest are affected. The standard deviation of these changes is less than 1%, but of course occurs only near shadow boundaries, where interpolation of the horizon is most important in determining the illumination. Those areas are critical in the determination of PSRs and in the characterization of high-illumination areas, so the use of the full elevation map database is warranted.

3.3. Average illumination

We calculated average illumination maps over several lunar node precession cycles (each 18.6 years). We used the DE421 ephemeris (Williams et al., 2008), whose approximate time span is 1900–2053. The simulations were run over four precession cycles from 1970 to 2044, with a time step of 6 h (i.e., ~109,000 frames total). For each pole, we obtain three maps: average Sun visibility (mean of the boolean Sun visible/not visible), average Sun illumination (mean of the normalized solar disc area visible), and average solar incident flux (similar to the previous one, but

modulated by the cosine of the incidence angle at each time step; it does not include the solar constant).

Fig. 6 shows the average Sun illumination of each pole over those precession cycles. Section 4 will address the PSRs, but we note that below 85°, previously unmodeled, large areas are mostly shadowed. Many of the small patches near the poles which have a high average were previously identified by Bussey et al. (1999), Bussey et al. (2005), Noda et al. (2008) and Bussey et al. (2010), with a closer match with the latest two, which also used recent laser altimeter-based topographic maps. In Section 5 we study those sites in further detail. We note that previous computations were limited (to ~5.5 years and to 1 year for Noda et al. (2008) and Bussey et al. (2010), respectively), except for very high-illumination regions, and did not cover a full precession cycle.

3.4. Earth visibility

While not a primarily scientific question, the visibility of the surface from Earth can have implications for future lunar exploration, whether human or robotic. We calculate the average visibility from Earth. The same elevation maps can be readily used; only the radius and location of the source need to be changed in the modeling second step. We consider the average Earth visibility (not illumination), i.e., we consider the Earth visible if any fraction of the disc is. From an exploration perspective, it means that we
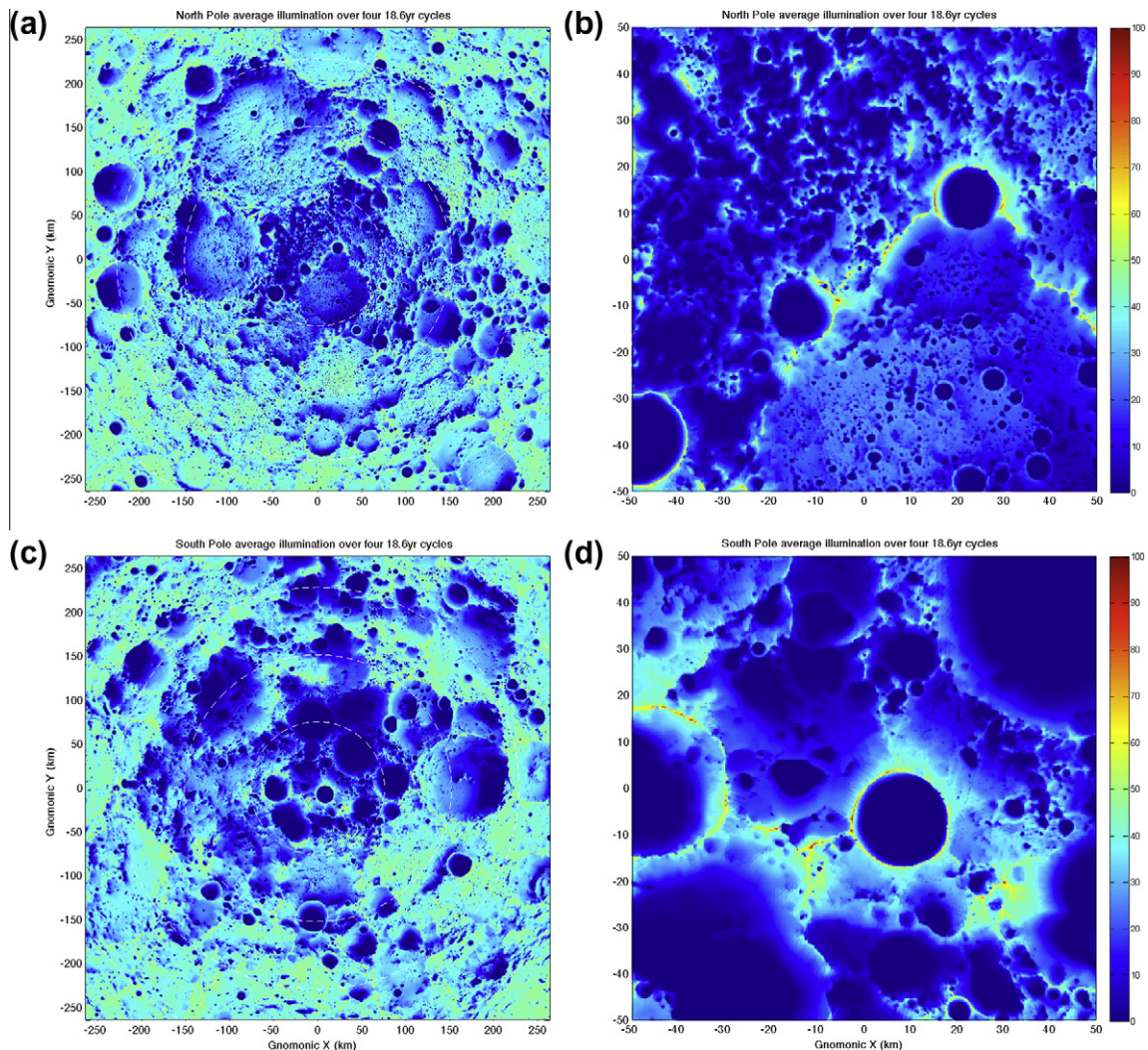
Fig. 6. Average illumination (in percent) for the north and south polar regions. The projection is polar gnomonic. (a,c) extend to ~80°; (b,d) extend to ~88°.
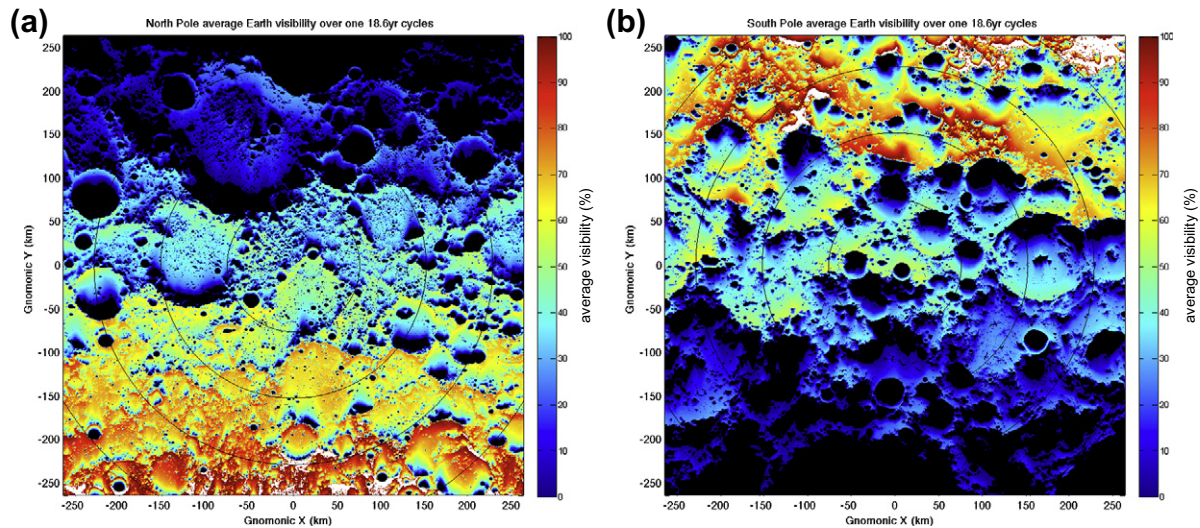
Fig. 7. The average visibility of Earth (in percent) for the north (a) and south (b) polar regions. Full visibility and total lack of visibility are indicated by white and black respectively.

consider tracking stations cover the globe fully, or that Low-Earth Orbit assets can be used for communication as well. Considering only the coverage by the NASA Deep Space Network sites could be important for the design of lander missions with specific communication requirements (see Fig. S2).

Fig. 7 shows the results of a simulation over one precession cycle. Because of the higher altitude range near the south pole, some high-latitude regions have good Earth visibility (e.g. Mons Malapert), compared to the north pole. Depending on specific power constraints, Mons Malapert may not be suitable for the location of a Moon base (as argued by Lowman et al. (2008)), but it could serve as a relay station to a large number of sites with extremely high illumination, such as the rim of Shackleton, which is visible from Malapert. The massif to the west (to the right of Malapert in Fig. 7) also has excellent visibility, as well as high illumination. In mission design, both Sun illumination and Earth visibility maps can be combined, and weighted depending on the mission requirements, to select potential candidate sites.

4. Permanently shadowed regions

Bistatic radar experiments with the Clementine spacecraft (Nozette et al., 1996) identified regions of high reflectivity in the lunar polar regions. Similar radar observations were made for Mercury (Margot et al., 1999). This spurred interest in PSRs, seen as potential cold traps of volatiles. Given the near-zero inclination of both bodies with respect to the Sun, sunlight never reaches directly the floor of deep craters near the poles. Observations by Lunar Prospector (Feldman et al., 2000) corroborated the relationship between PSRs and estimated volatile abundances. Recently however, this link has been questioned by new measurements (Mitrofanov et al., 2010a,b) by the LEND instrument onboard LRO (Mitrofanov et al., 2010c).

4.1. Extent

PSRs were identified from spacecraft images (Nozette et al., 1996), and modeling from radar-derived topography (Margot et al., 1999). However, the limited time period of robotic observations and the large areas invisible from Earth made it problematic to conduct a thorough survey of PSRs. Noda et al. (2008) were the first to use reliable high-resolution polar topography to determine the extent of those permanently shadowed regions. However, their

study region extended to only 5° from the poles, and as a consequence they underestimate the surface area of present-day PSRs. Bussey et al. (2010) also had a restricted study region (86–90°S).

In order to characterize PSRs, regions where the Sun has not directly shone since the distant past (e.g., millions of years and more), we performed another simulation which does not reflect any given time period. We define the PSRs as the areas that never receive direct solar illumination. As shown in Section 4.2, those regions actually all receive indirect (scattered) light (in addition to starlight). Although during the previously simulated four precession cycles (Section 3.3), the sub-solar latitude nearly reached its extrema over the whole longitude range, this new simulation holds it fixed at its maximum or minimum (for the north and south, respectively) value, over all longitudes. This artificial maximum illumination month gives the most restrictive extent of zero-illumination regions. That is, the areas which are never illuminated in the simulation are expected to be PSRs, at the current lunar obliquity. We selected the value of this sub-solar latitude extremum from the DE421 ephemeris ($i = 1.5863°$). The solar longitude step is 0.25°, which would correspond to about 30 min in a real month. We note that differences with the 4-cycle results are very small. In the south, the maximum-case results show 2.58% more area in permanent shadow than the temporal simulation (corresponding to 0.07% of the total area).

Fig. 8 presents the PSRs in the region, obtained from the maximum illumination simulations. In each polar region, the largest 150 PSRs are emphasized (in red[2] in Fig. 8; the smaller PSRs are in cyan). We exclude the smallest shadowed regions (less than 9 contiguous pixels) from our sample. Those are more susceptible to artifacts due to small errors in the topographic model, and are probably not significant enough for potential volatile storage. Nevertheless, uncertainties in the topography are unlikely to affect the results below.

The total PSR area is 12,866 km^2 in the north and 16,055 km^2 in the south (respectively 4.7% and 5.8% of the total region area). This is significantly higher than simulated topography predictions by Bussey et al. (2003), who estimated total PSR areas of 12,500 and 6500 km^2 over larger regions (polewards of 78°). Areas in sequentially smaller polar regions are listed in Table 1. Compared to

---

[2] For interpretation of color in Fig. 8, the reader is referred to the web version of this article.
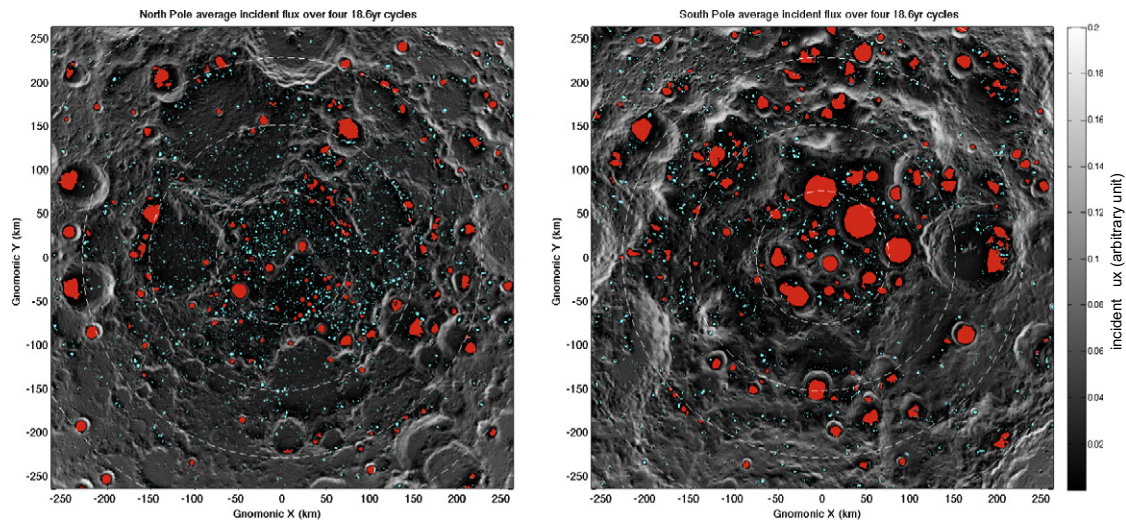
Fig. 8. Permanently shadowed regions shown in color over a grayscale map of the average incident flux over four precession cycles. For each pole (a, north; b, south), the red color indicates the 150 largest PSRs. The smaller PSRs are displayed in cyan. (For interpretation of the references to colours in this figure legend, the reader is referred to the web version of this paper.)

Table 1
Area in permanent shadow calculated over the whole region and in several pole-centered areas with comparison to previous studies, for both the south and north polar regions.

	North	South
>78° Bussey et al. (2003)	12,500	6500
Whole region (∼80°)	12,866	16,055
>82.5°	8881	12,202
>85°	4764	7024
>85° Noda et al. (2008)	1236	4466
>87.5°	1769	3660
>87.5° Noda et al. (2008)	844	2751
>87.5° Margot et al. (1999)	1030	2550
>87.5° Nozette et al. (1996)	530	6361
>87.5° > 1 km²	1665	3632
>87.5° > 2 km²	1496	3588
>87.5° > 5 km²	1236	3516
>87.5° > 10 km²	983	3397
>87.5° > 25 km²	575	3306
>87.5° > 50 km²	523	3187

the smaller spatial extent of the DEMs used by Noda et al. (2008): in their Fig. 3, the largest PSRs (Haworth, Shoemaker, Faustini, Sverdrup, de Gerlache, and Shackleton) do not show a well-defined outline, such as in our Fig. 8. Bussey et al. (1999) obtain a much larger value: 3300 km² above 88.5°S, compared to our 855 km². The topographic model used by Bussey et al. (2010) included additional altimetric profiles compared to the Noda et al. (2008) study, but had a similar horizontal resolution (474 m). Their total PSR area above 86° (5058 km²) is also significantly smaller than our results (6096 km² over the same region). Fig. S3 presents further details on the different PSR distribution in both polar regions.

Finally, Table 2 gives the distribution of PSRs by size and latitude. As shown in Fig. 8, the north pole has a large number of small PSRs at high latitude, while in the south larger regions contribute more, and almost exclusively nearest the pole.

4.2. Estimation of scattered flux in PSRs

While the PSRs identified above are never illuminated by the Sun directly, light scattered from neighboring topography contributes to their energy and thermal balance. The impact of those different topographic environments can be quantified by the model presented in Section 2.3. We do not intend to fully model the effects of this scattered light on potential volatiles present in the PSRs, but we can recognize qualitative and quantitative differences between the various PSRs, which could be of interest to future

previous studies (only possible above 87.5°: Noda et al., 2008; Margot et al., 1999; Nozette et al., 1996; Bussey et al., 1999), our values tend to be substantially larger. In the north pole region, the 844 km² value of Noda et al. (2008) could be reconciled by our improved resolution of the topographic model (240 m vs. 470 m), enabling PSRs 10 km² and smaller to be characterized. In the south however, this same resolution effect cannot be invoked, and we attribute the large discrepancy to the visible artifacts and

Table 2
Size distribution of PSRs with their center latitude, for both poles.

	North pole					South pole				
	>80°	>82.5°	>85°	>87.5°	>89°	>80°	>82.5°	>85°	>87.5°	>89°
>1 km²	1457	1199	773	272	42	892	609	280	92	15
>5 km²	344	273	159	68	10	314	220	96	39	8
>10 km²	182	134	77	31	4	177	116	55	21	3
>25 km²	68	45	18	5	2	91	63	30	14	3
>50 km²	37	22	9	3	2	59	43	22	II	3
>100 km²	17	7	2	1	0	30	25	13	5	1
>200 km²	7	4	1	1	0	13	II	8	4	1
>400 km²	0	0	0	0	0	4	4	4	2	0
>600 km²	0	0	0	0	0	3	3	3	1	0
>1000 km²	0	0	0	0	0	2	2	2	1	0

(a)

North Pole : scattered flux in the largest PSRs

(b)

North Pole : scattered flux in the largest PSRs
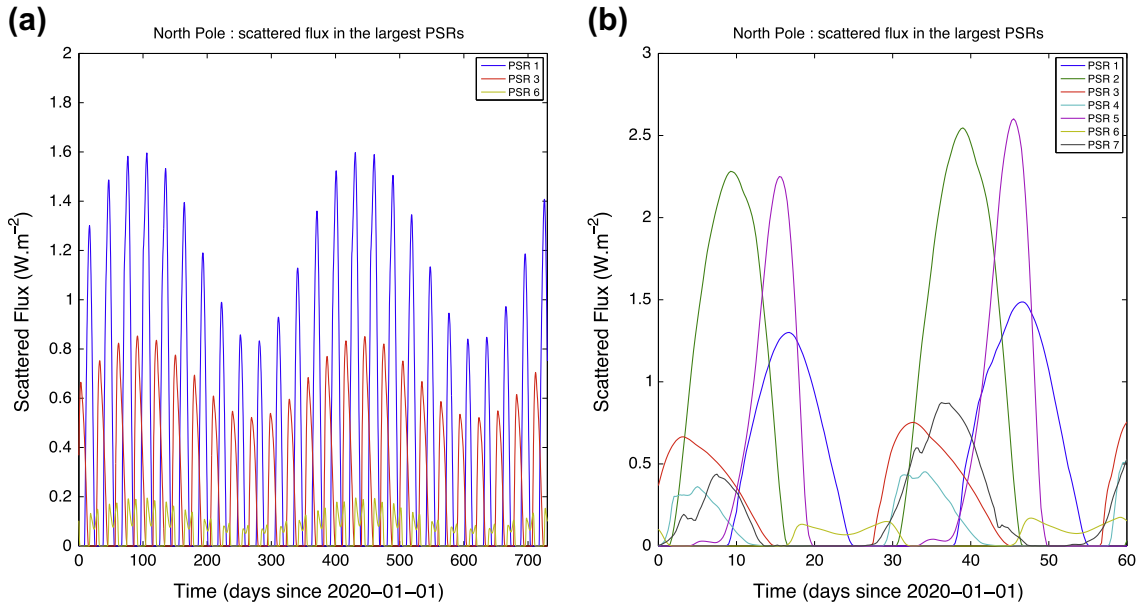
Fig. 9. Time series of flux scattered into the largest north pole PSRs by surrounding topography, over two years (a) and two months (b) to highlight the quantitative and qualitative variability.

(a) North Pole average scattered flux (W.m^{-2}) over one 18.6yr cycle

(b) South Pole average scattered flux (W.m^{-2}) over one 18.6yr cycle

(c) North Pole maximum scattered flux (W.m^{-2}) over one 18.6yr cycle

(d) South Pole maximum scattered flux (W.m^{-2}) over one 18.6yr cycle
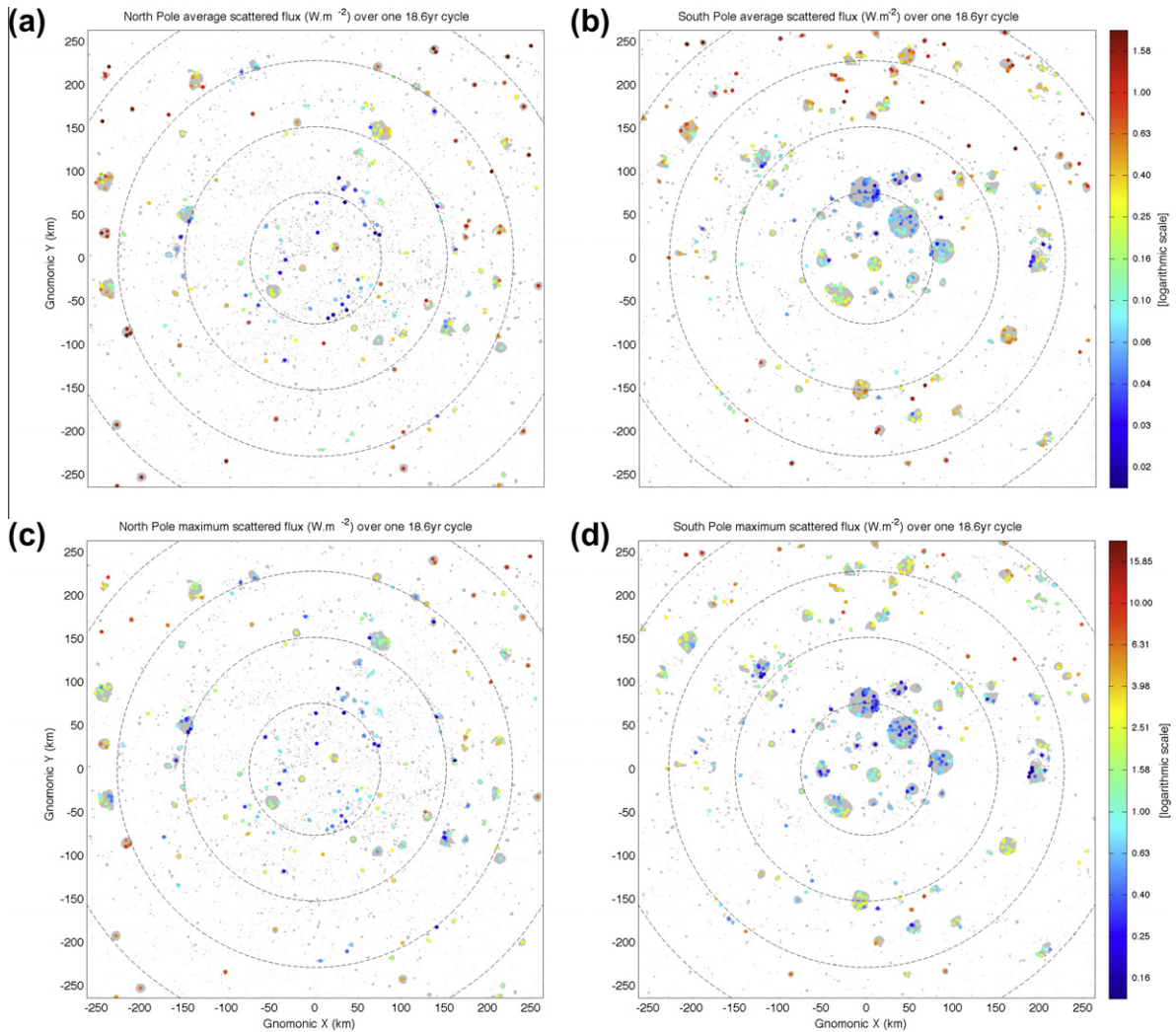
Fig. 10. Average (a, b) and maximum (c, d) scattered flux calculated at all the representative points selected within the 150 largest PSRs in each polar region. Warmer colors indicate larger incident scattered flux. Note that the logarithmic colorscale differs by one order of magnitude between average and maximum maps.

focused studies. We assume a constant surface albedo of 0.12, and a solar constant of 1366 W m^{-2}.

In each polar region, we selected representative points of the largest 150 PSRs (see Fig. 8; the smallest is ~12 km^2). In order to account for spatial variability of the incoming scattered flux in the largest PSRs, multiple points were randomly distributed inside of those (depending on their area, up to 12 and 32 points in the north and south respectively).

The scattered flux was calculated over one precession cycle (starting in January 2010) with a time step of 6 h for each of the chosen locations (225 and 399 respectively in the north and south). Fig. 9 shows examples of the obtained scattered flux time series for a few of the largest PSRs in the north polar region. They receive scattered light in a monthly cycle (scattered day and night), whose phasing changes because of their longitude, and the amount varies significantly (e.g., PSR1 vs. PSR6). We find that every PSR, at both poles, receives some amount of indirect illumination over the year. Even though small craters inside of larger PSRs might not receive singly-scattered light (our representative points are a limited sample), this indicates that, especially on long timescales, scattered light is important for the thermal balance of PSRs.

We characterize each location by the average and maximum of its scattered flux. In Fig. 10, we present the spatial variability of the average and maximum scattered flux in both polar regions, both can be relevant to volatile escape/sublimation (Vasavada et al., 1999). This study finds that all PSRs do get some scattered light. There is a clear latitudinal trend, with near-polar PSRs receiving significantly less (more than one order of magnitude) scattered flux than PSRs at lower latitudes. The walls of large craters (the major scatterers) are receiving less direct illumination flux, and are more likely to be shadowed.

In the case of the north pole, this could be enhanced by the large Peary crater. For a given value of the average scattered flux, bigger PSRs have a smaller maximum scattered flux (Fig. 11a). This can have implications on peak sublimation rates, and means that PSRs in large flat-floored basins get little scattered energy input, even when only part of the floor is in permanent shadow (Paige et al.,

2010). In the north, out of the seven major PSRs (Sylvester, Lovelace, Lenard, and four unnamed craters), the Lenard PSR is the darkest.

In the south, the scattered flux difference between PSRs due to their size is not as clear from Fig. 11b, where two distinct populations are not visible, even though the largest PSRs near the poles generally receive low amounts of scattered light. Fig. 10 also shows the different qualitative scattered light environment in the southern large PSRs. Because those are larger and closer to the pole, they are darker than in the north.

We also characterized the scattered flux at the LCROSS impact site (311.281°E, 84.675°S). As shown in the inset of Fig. 11b, the LCROSS impact site is among the "darkest" locations in our result sample. We find an average flux of 24.8 ± 1.3 mW m^{-2} and a maximum flux of 172.5 ± 16.0 mW m^{-2}. The Cabeus PSR has lower maximum values than other PSRs with similar average flux. This is in good agreement with results from the Diviner instrument (Paige et al., 2010), who found the LCROSS impact site to be one of the coldest locations in the south pole region for present lunar orientation. In addition, Cabeus also has the highest hydrogen content in the south polar region (Mitrofanov et al., 2010a,c).

5. Study of maximum illumination areas

5.1. Sites of maximum illumination

As noted by Bussey et al. (1999, 2003) and Noda et al. (2008) and earlier studies, the high crater rims close to the poles record the highest illumination values. Although more of the vicinity of the south pole is in permanent shadow, the large topography range responsible for this enables generally better illumination for those high points than in the north.

From the results of the long temporal simulation (Section 3.3, Fig. 6), we identified the 50 grid elements with largest average solar illumination in each polar region. Table 3 presents the statistics for the 50 most illuminated locations in both poles. In the south, the site with the most illumination is also the one with the best
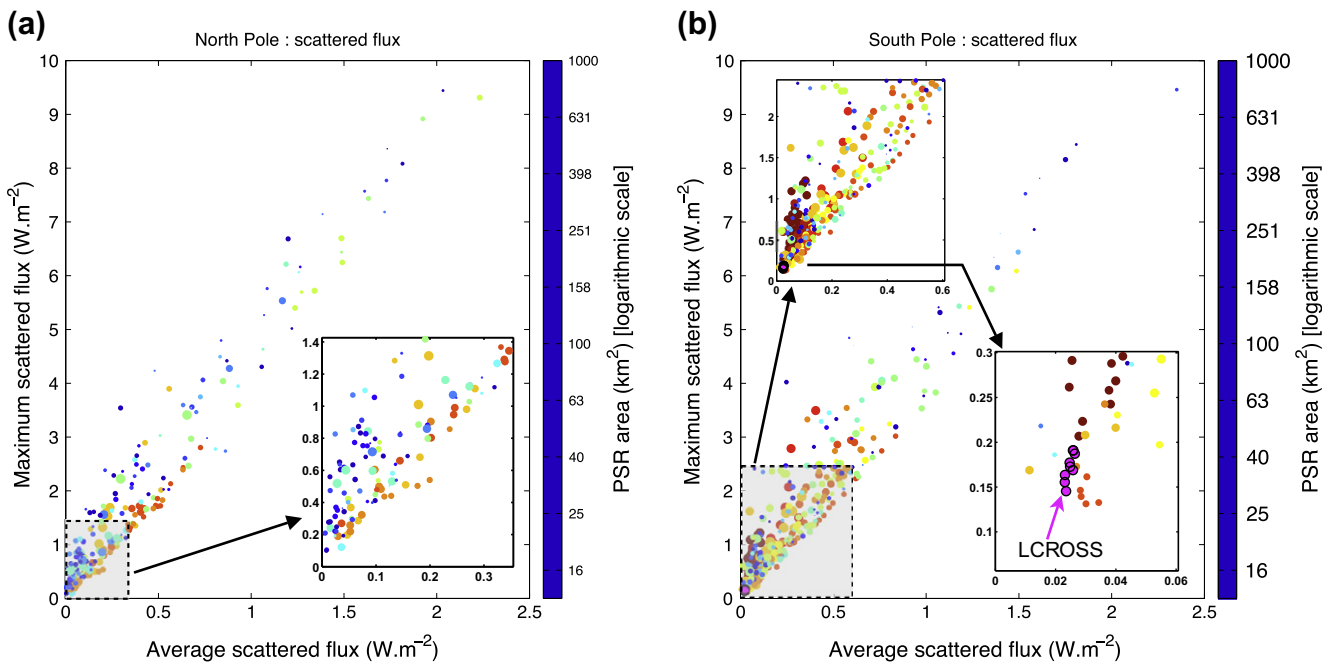
Fig. 11. Scatter plot of the maximum of the scattered flux versus its average. Color indicates, in a logarithmic scale, the size of the PSR to which the calculation point belongs. Note the different color scale between both poles. The size of the symbols is related to the latitude (larger means closer to the pole). Points near the LCROSS impact site are specially marked.

Table 3
List of the 50 most illuminated spots in each pole. In addition to their location (longitude, latitude), we indicate their average illumination and visibility percentage at the surface and 10 m above the surface. Due to this height increase, their rank can change.

Longitude	Latitude	At surface level			10 m above surface		
		Rank	Average solar illumination (%)	Average solar visibility (%)	Rank	Average solar illumination (%)	Average solar visibility (%)
North pole							
242.24	88.06	1	86.08	89.39	3	86.36	89.69
126.80	89.37	2	84.56	89.44	2	86.42	91.42
126.21	89.38	3	84.48	89.41	6	85.83	90.80
131.09	89.34	4	84.40	89.57	10	85.30	90.37
130.56	89.35	5	84.01	89.17	12	85.15	90.21
127.94	89.36	6	83.87	88.83	1	86.63	91.57
125.62	89.38	7	83.38	88.47	11	85.21	90.21
242.03	88.05	8	82.49	85.45	6	85.83	89.05
7.22	87.20	9	82.16	84.67	23	82.29	84.75
128.94	89.36	10	82.02	87.25	13	84.83	90.23
130.03	89.35	11	81.76	87.20	14	84.70	89.87
7.20	87.19	12	81.68	84.22	24	82.26	84.71
232.04	87.31	13	81.55	83.99	27	81.65	84.09
231.93	87.31	14	81.11	83.93	28	81.58	84.03
7.24	87.21	15	80.92	83.95	25	82.21	84.70
128.38	89.37	16	80.71	86.08	20	84.08	89.42
242.44	88.06	17	80.68	85.48	4	86.18	89.64
326.13	89.65	18	80.61	86.85	17	84.49	90.44
129.49	89.36	19	80.49	85.73	19	84.18	89.45
127.37	89.37	20	80.57	85.43	8	85.56	90.40
131.61	89.34	21	80.43	85.93	22	83.81	89.06
7.04	87.13	22	80.33	83.09	32	81.21	83.69
8.09	86.99	23	80.03	82.59	38	80.40	82.91
7.17	87.12	24	79.84	82.43	30	81.33	83.81
7.96	87.00	25	79.72	82.31	39	80.20	82.76
7.94	86.99	26	79.69	82.28	40	80.18	82.75
8.11	87.00	27	79.53	82.11	41	79.92	82.51
327.23	89.66	29	79.43	85.80	18	84.22	90.52
242.13	88.06	28	79.44	84.81	5	86.10	89.36
242.33	88.07	30	79.32	83.92	9	85.47	89.54
242.54	88.07	31	79.06	83.57	15	84.69	89.05
133.11	89.32	32	78.95	84.54	35	81.03	86.64
325.39	89.66	33	78.93	85.62	16	84.55	90.57
133.59	89.32	34	78.70	84.28	33	81.11	86.77
110.38	89.85	35	78.09	84.97	43	79.10	86.00
132.61	89.33	36	78.04	83.53	36	80.83	86.40
7.78	87.05	37	77.87	80.65	44	78.90	81.65
109.36	89.84	38	77.55	84.34	45	78.76	85.75
327.93	89.65	39	77.35	83.00	21	84.04	89.87
132.11	89.33	40	77.20	82.57	31	81.24	86.80
111.19	88.96	41	77.16	82.83	46	78.19	83.45
7.80	87.06	42	77.04	79.67	48	78.13	80.99
7.02	87.12	43	76.94	81.07	34	81.04	83.55
232.17	87.31	44	77.06	80.24	29	81.52	83.98
302.36	87.21	45	76.80	79.55	49	77.10	79.82
125.02	89.39	46	76.70	81.60	37	80.69	85.93
111.60	88.96	47	76.66	81.94	47	78.18	83.47
302.45	87.22	48	76.69	79.54	49	77.10	79.81
7.05	87.20	49	76.62	81.76	26	82.14	84.65
8.07	86.99	50	76.51	78.38	42	79.73	82.30
South pole							
222.69	−89.45	1	89.01	92.66	1	93.10	95.83
222.73	−89.43	2	88.60	91.14	2	92.53	95.24
223.28	−89.44	3	87.13	90.04	3	92.26	94.95
204.27	−89.78	4	86.71	90.46	12	87.41	90.99
203.46	−89.77	5	86.70	90.43	11	87.42	91.00
37.07	−85.30	6	85.95	89.43	14	87.30	89.52
123.64	−88.81	7	85.50	88.20	21	85.59	88.29
197.05	−89.69	8	85.28	88.77	20	85.93	89.33
222.14	−89.44	9	85.20	89.68	4	91.86	94.77
37.01	−85.30	10	84.81	87.65	13	87.33	89.53
291.90	−88.67	11	84.61	87.64	27	84.74	87.74
198.43	−89.69	12	84.44	88.08	23	85.19	88.70
202.69	−89.76	13	83.74	87.67	16	86.88	90.63
222.59	−89.47	14	83.68	87.98	6	89.57	93.39
223.25	−89.45	15	82.73	86.88	5	91.82	95.83
291.58	−88.68	16	82.50	86.08	28	84.68	87.70
205.14	−89.79	17	82.37	86.42	19	86.19	90.14
37.57	−85.55	18	82.34	85.52	38	82.62	85.78
123.95	−88.80	19	82.37	85.04	26	84.92	87.82

Table 3 (continued)

Longitude	Latitude	At surface level			10 m above surface		
		Rank	Average solar illumination (%)	Average solar visibility (%)	Rank	Average solar illumination (%)	Average solar visibility (%)
31.73	−85.43	20	82.22	85.76	33	83.32	86.66
37.00	−85.31	21	81.96	86.92	15	87.25	89.47
196.63	−89.68	22	81.99	85.76	24	85.14	88.85
357.70	−85.97	23	81.76	84.43	37	82.66	85.23
291.77	−88.67	24	81.67	84.55	30	84.05	87.14
223.21	−89.46	25	81.61	85.60	7	89.33	93.27
222.54	−89.48	26	81.59	86.23	9	87.58	91.40
205.25	−89.77	27	81.04	85.33	18	86.23	89.96
357.59	−85.96	28	80.85	83.23	35	82.70	85.12
198.90	−89.69	29	80.78	85.02	31	83.99	87.93
356.80	−85.96	30	80.61	83.09	40	82.27	84.81
37.59	−85.54	31	80.56	83.62	39	82.29	85.44
357.58	−85.97	32	80.56	83.66	35	82.70	85.25
1.87	−86.00	33	80.49	83.19	32	83.47	86.04
292.19	−88.59	34	80.38	83.44	43	80.84	83.92
123.43	−88.80	35	80.40	83.61	22	85.39	88.20
223.32	−89.43	36	80.28	83.18	10	87.52	89.79
223.17	−89.47	37	80.27	85.22	8	88.22	92.00
31.81	−85.42	38	80.21	83.34	42	82.17	85.80
37.09	−85.29	39	80.11	82.87	17	86.37	88.42
292.31	−88.59	40	79.85	83.00	44	80.52	83.55
221.89	−89.48	41	79.64	83.94	25	84.95	88.82
243.65	−85.83	42	79.59	82.24	48	79.85	82.30
37.65	−85.55	43	79.70	82.68	40	82.27	85.39
243.22	−85.73	44	79.54	82.28	46	80.00	82.43
243.32	−85.73	45	79.36	82.27	47	79.96	82.39
197.49	−89.70	46	79.32	83.92	34	83.28	87.30
243.41	−85.68	47	79.24	81.60	49	79.76	82.00
221.23	−89.49	48	79.11	83.34	29	84.24	88.14
243.60	−85.83	49	79.13	82.16	50	79.58	82.23
356.80	−85.97	50	78.85	81.62	45	80.50	83.27
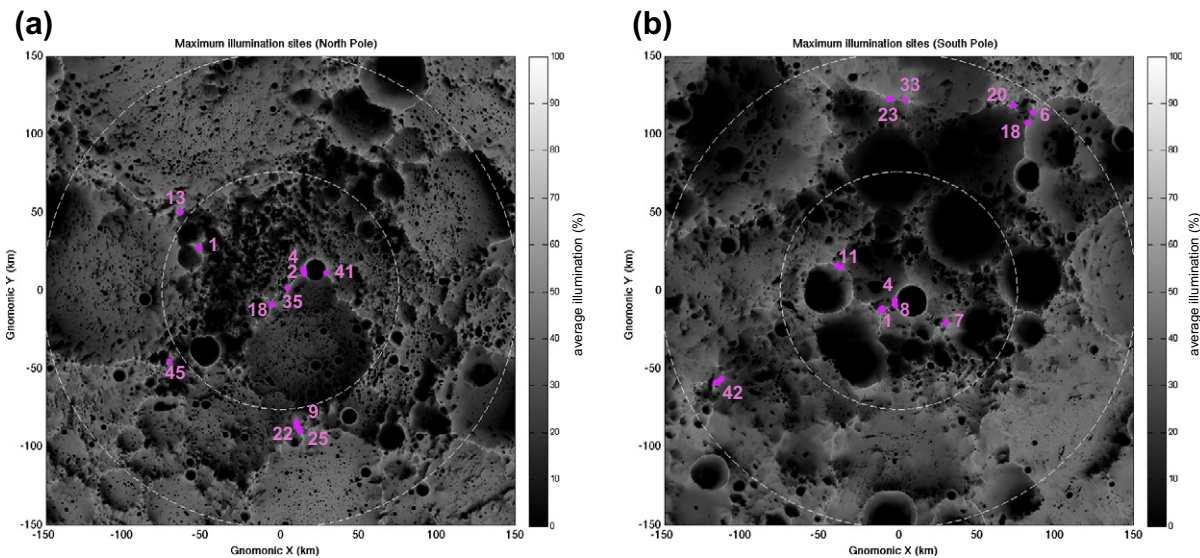
Fig. 12. Sites of maximum illumination in the north (a) and south (b) polar regions, over a grayscale map of average sun illumination. The numbers indicate the rank at surface level found in Table 3; only the best-illuminated point in each cluster is labeled.

Sun visibility, but it is not the case in the north. These are distributed in 8 and 10 clusters, respectively in the north and south (Fig. 12).

In the north, we find that the point with the maximum average illumination at the surface is at 88°N, compared to 89.5°S in the south. Nevertheless, it is in the south pole region that lower-latitude locations, with potentially better Earth visibility, display the highest values.

Noda et al. (2008) obtained total areas with more than 80% average Sun visibility of 1 and 5 km² in the north and south respec-

tively. Above 80° latitude, which corresponds to their analysis region, we find 3.34 and 5.01 km², respectively (that is, 58 and 87 grid elements). However, when we use the same 80% criterion for the average Sun illumination (i.e., taking into account how much of the solar disc is visible), those numbers decrease to 1.32 and 2.25 km² (i.e., 23 and 39 grid elements). See Table S1 for more detail. We find a well-illuminated site (our 7th best) near the best location reported by Bussey et al. (2010) (124.5°E, 88.74°S), with similar average illumination (85.5% vs. 86%). However, our best illuminated sites lie closer to other points reported by Bussey
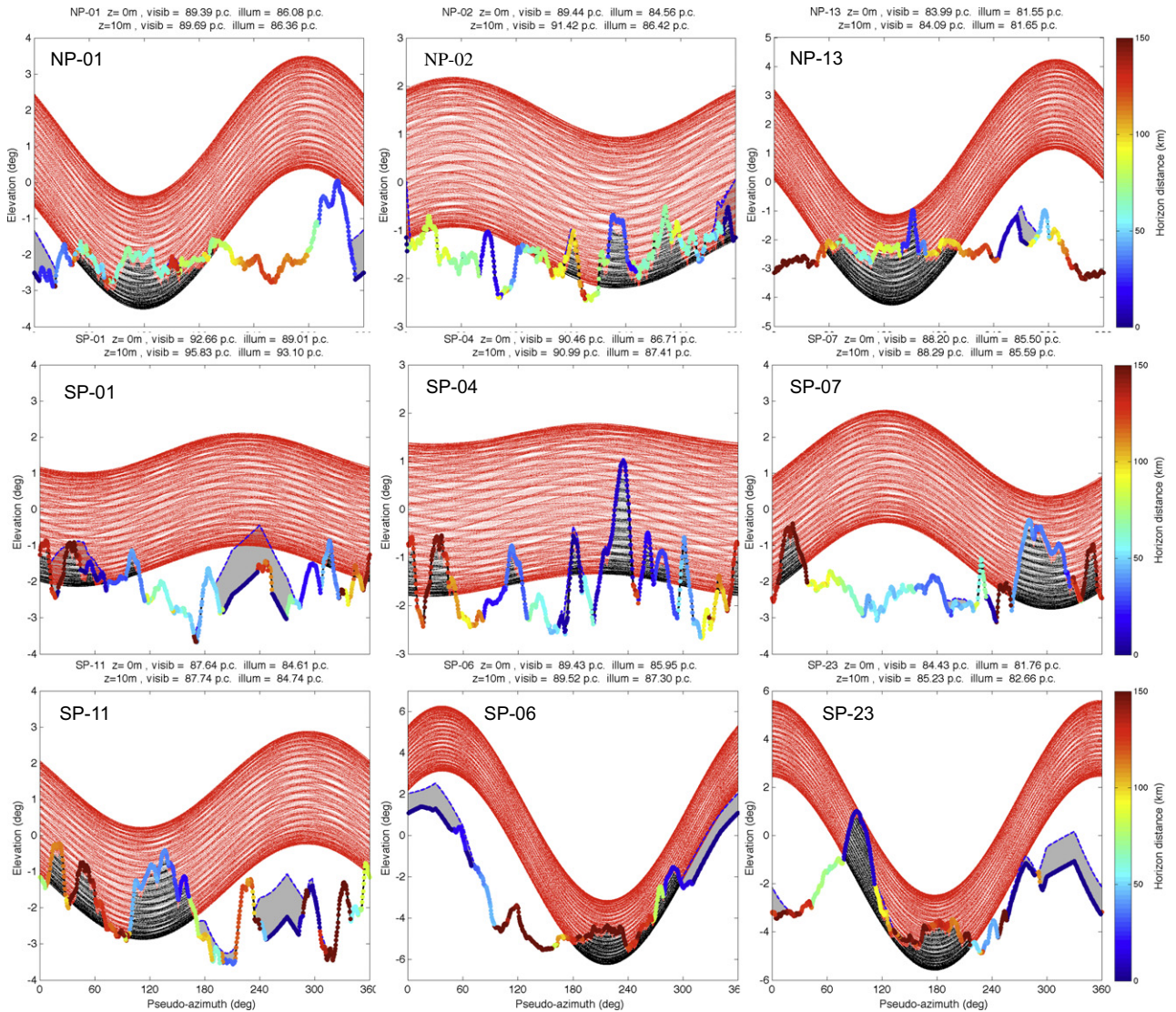
Fig. 13. Illustration of the modeled average illumination for selected locations among the best-illuminated in each polar region. The horizon elevation is shown both at surface level (dashed blue line) and 10m above the surface, color-coded to indicate the distance to the obstacle on the horizon, from very local (dark blue) to 150km away (red).The path of the sun over for precession cycles is indicated by small dots (at 6h intervals), which are red when the sun is visible (even partially, when slightly below the horizon) and black when it is completely occulted.

et al. (2010), in their Table 2. These discrepancies could be due to the difference in simulation duration and accuracy (their time step is 12 h), and the extent of the topographic model used. The padding around their region of interest (86–90°S) is only 1° (85–86°S), compared to 5° in this work.

5.2. Effects of local topography, and implications for lunar exploration

While the Sun blocking elements in the horizon of the best-illuminated regions are often distant, the very local topography can be part of the obstacle. The maps used above (Fig. 6) can be useful to discern the locations most susceptible to high solar resources, but they were obtained at surface level.

Solar panels mounted on high towers (hundreds of meters) have been proposed to improve the surface illumination conditions (Fincannon, 2008), but we find that very small height changes can dramatically improve already-favorable locations. Additional columns in Table 3 show the values of average illumination and visibility at 10 m altitude. That such small height changes can be that beneficial to average illumination was unex-

pected. Further (appreciable) increases only occur for much larger heights.

Fig. 13 shows the horizons, at surface level (dashed) and 10 m altitude (color is mapped to the horizon distance), of selected points at sites indicated in Fig. 12 (and Table 3). The calculations were done on one precession cycle starting in 2020. The surface-level horizon is only visible (shaded gray) when the 10 m height change helped the local topography obstacle to be reduced, or disappeared. The smoothness of the dashed line is indicative of the effect of interpolation of local topography during the horizon calculation. While sites NP-01, NP-13, SP-04, SP-07, SP-11, SP-06 and SP-23 do not benefit significantly from the increased altitude, because their horizon-blocking topographic obstacles are distant, the sites NP-02 and SP-01 have their "night" durations and occurrences reduced.

We illustrate this with the best-illuminated location on the Moon (SP-01: 222.69°E, 89.45°S). Fig. 14a–c shows the time series of illumination, at the surface (blue) and at 10 m altitude (red). At this location, at surface level, every year has a period of 202 ± 7 days of total, uninterrupted sunlight, and 339 sunlit days per year (326 of those have full Sun visibility, compared to 307
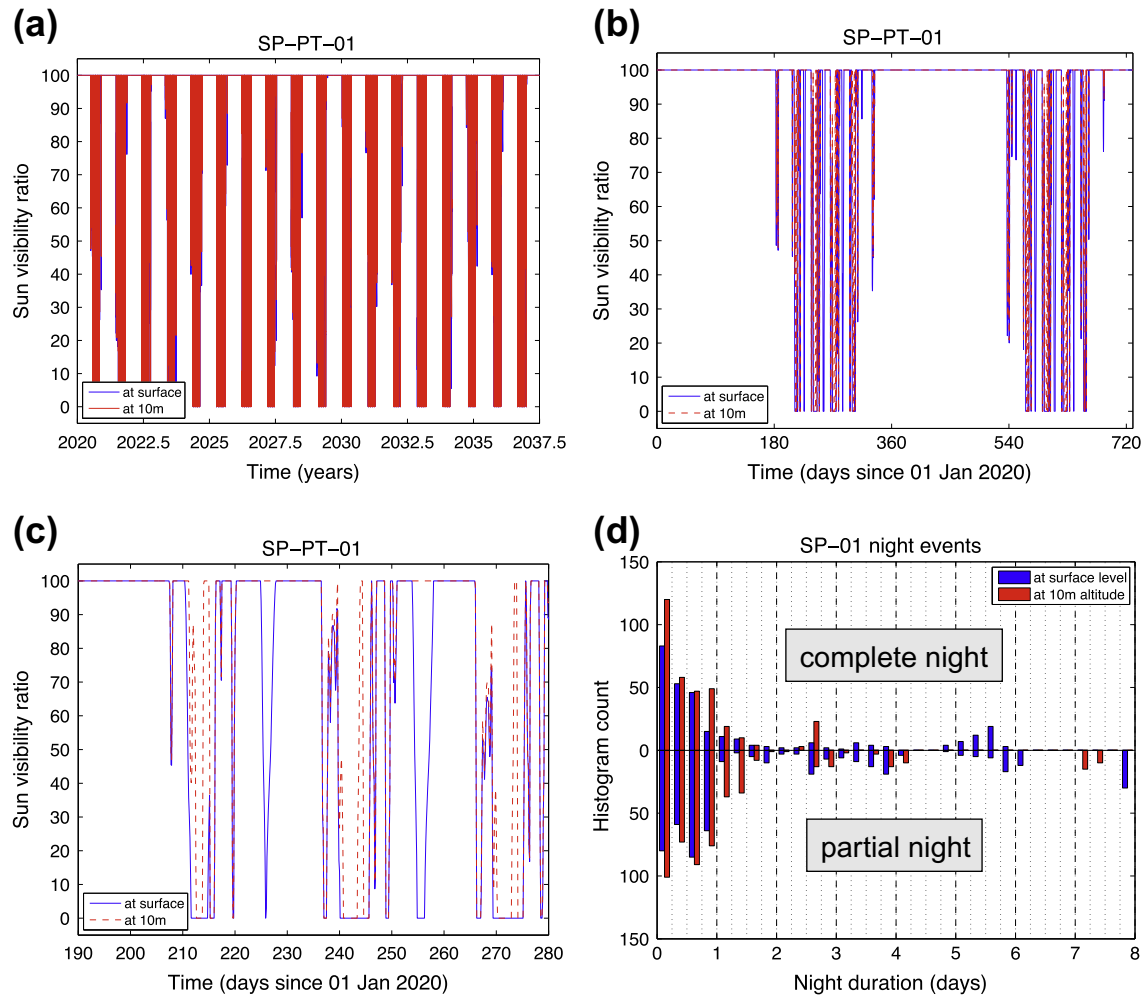
Fig. 14. (a–c) Time series of the sun visibility ratio from the best-illuminated spot on the Moon, at surface level (blue) and at 10m altitude (red). (d) Histogram of the duration of partial and total sun occlusion. 12. (For interpretation of the references to colours in this figure legend, the reader is referred to the web version of this paper.)

at surface level). The longest period with solar illumination (even partial) is 261 days over the precession cycle. Fig. 14d shows that the height change helps reduce number of Sun occultations, and their duration. The durations of the long days increase only slightly to 204 ± 8 days, and there are 350 sunlit days. However, in Fig. 14c, one can also note that some instances of multiple-day night events can be completely avoided at 10 m altitude. Critically, the longest total night at the surface is 5.88 days, but only 2.75 days at 10 m, while the longest partial nights are respectively 10.5 and 7.4 days. Table S2 gives the day/night statistics of the 100 points of Table 3, relevant for mission planning.

6. Conclusions

In this work, we showed that the altimetric data collected by the LOLA instrument can be used to model precisely the illumination conditions of the lunar polar regions. Characterization of the lunar poles to understand the existence and history of volatiles is one of the primary objectives of the Lunar Reconnaissance Orbiter exploration-phase mission (Chin et al., 2007). Such information is critical for future surface mission planning, in terms of usable power source, and thermal and power constraints. Communication potential with the Earth can be assessed very similarly.

In addition, the use of the horizon method permits high-resolution simulations (both spatially and temporally) over long time spans. We characterized PSRs over a larger region than previous studies, and extended our method to assess the singly-scattered flux environment in those regions. We find that all PSRs do receive indirect illumination over on year. Over long timescales, this scattered flux can be important for volatile stability at the surface.

We also identified various sites with high solar illumination at the surface level. We find that some of those locations can greatly benefit from modest elevation changes, such as beam-mounted solar panels.

The elevation map database resulting from this work can be easily used in further mission concept analysis for power and communication constraints (e.g., International Lunar Network, G. Tahu, personal communication) and in surface activity route planning with biometric and power constraints (Johnson et al., 2010a; Johnson et al., 2010b).

Appendix A. Supplementary material

Supplementary data associated with this article can be found, in the online version, at doi:10.1016/j.icarus.2010.10.030.

References

Acton, C.H., 1996. Ancillary data services of NASA's navigation and ancillary information facility. Planet. Space Sci. 44, 65–70.

Araki, H. et al., 2009. Lunar global shape and polar topography derived from Kaguya-LALT laser altimetry. Science 323, 897–900. doi:10.1126/science.1164146.

Archinal, B.A., Rosiek, M.R., Kirk, R.L., Redding, B.L., 2006. The Unified Lunar Control Network 2005. US Geological Survey Open-File Report 2006-1367.

Arnold, J.R., 1979. Ice in the lunar polar regions. J. Geophys. Res. 84, 5659–5668.

Bryant, S., 2010. Lunar Pole Illumination and Communications Statistics Computed from GSSR Elevation Data, SpaceOps 2010 Conference, Huntsville, Alabama, Abstract AIAA-2010-1913.

Bussey, D.B.J., Spudis, P.D., Robinson, M.S., 1999. Illumination conditions at the lunar south pole. Geophys. Res. Lett. 9, 1187–1190.

Bussey, D.B.J., Lucey, P.G., Steutel, D., Robinson, M.S., Spudis, P.D., Edwards, K.D., 2003. Permanent shadow in simple craters near the lunar poles. Geophys. Res. Lett. 30, 1278. doi:10.1029/2002GL016180.

Bussey, D.B.J., Fristad, K.E., Shenk, P.M., Robinson, M.S., Spudis, P.D., 2005. Constant illumination at the lunar north pole. Nature 434, 842. doi:10.1038/434842a.

Bussey, D.B.J., McGovern, J.A., Spudis, P.D., Neish, C.D., Noda, H., Ishihara, Y., Sørensen, S.-A., 2010. Illumination conditions of the south pole of the Moon derived using Kaguya topography. Icarus, in press. doi:10.1016/j.icarus.2010.03.028.

Chin, G. et al., 2007. Lunar Reconnaissance Orbiter overview: The instrument suite and mission. Space Sci. Rev. 129. doi:10.1007/s11214-007-9153-.

Colaprete, A. et al., 2010. Detection of water within the LCROSS ejecta plume. Science 330, 463–468. doi:10.1126/science.1186986.

Cook, A.C., Watters, T.R., Robinson, M.S., Spudis, P.D., Bussey, D.B.J., 2000. Lunar polar topography derived from Clementine Stereoimages. J. Geophys. Res. 105, 12023–12033, doi:10.1029/1999JE001083.

Dozier, J., Burno, J., Downey, P., 1981. A faster solution to the horizon problem. Comput. Geosci. 7, 145–151.

Eliason, E., Isbell, C., Lee, E., Becker, T., Gaddis, L., McEwen, A., Robinson, M., 1999. Mission to the Moon: The Clementine UVVIS Global Lunar Mosaic, PDS Volumes USA_NASA_PDS_CL_4001-4078, Produced by the US Geological Survey and Distributed on CD Media by the Planetary Data System (Released 4/2000), <http://www.lpi.usra.edu/lunar/tools/clementine/instructions/UVVIS_DIM_Info.html>.

Feldman, W., Lawrence, D., Elphic, R., Barraclough, B., Maurice, S., Genetay, I., Binder, A., 2000. Polar hydrogen deposits on the Moon. J. Geophys. Res. 105, 4175–4195, doi:10.1029/1999JE001129.

Fincannon, J., 2008. Lunar Polar Illumination for Power Analysis, NASA/TM—2008-215446, <http://www.gltrs.grc.nasa.gov/reports/2008/TM-2008-215446.pdf>.

Garrick-Bethell, I., Byrne, S., Hoffman, J.A., Zuber, M.T., 2005. Areas of favorable illumination at the lunar poles calculated from topography. Lunar Planet. Sci. XXXVI, Houston, TX. Abstract #2006.

Gaskell, R.W. et al., 2008. Characterizing and navigating small bodies with imaging data. Meteorit. Planet. Sci. 43, 1049–1062.

Johnson, A.W., Hoffman, J.A., Newman, D.J., Mazarico, E.M., Zuber, M.T., 2010a. An Integrated EVA Mission Planner and Support Tool for Lunar Exploration. Poster Presented at the 2010 NASA Human Research Program Investigator's Workshop, Houston, TX, 3–5 February 2010.

Johnson, A.W., Hoffman, J.A., Newman, D.J., Mazarico, E.M., Zuber, M.T., 2010b. An Integrated EVA Mission Planner for Planetary Exploration, AIAA SPACE 2010 Conference & Exposition, Anaheim, CA, 30 August–2 September 2010.

Li, X., Wang, S., Zheng, Y., Cheng, A., 2008. Estimation of solar illumination on the Moon: A theoretical model. Planet. Space Sci., 947–950. doi:10.1016/j.pss.2008.02.008.

Lowman, P.D., Sharpe, B.L., Shrunk, D.G., 2008. Moonbase Mons Malapert? Making the Case, Aerospace America, October 2008.

Margot, J.L., Campbell, D.B., Jurgens, R.F., Slade, M.A., 1999. Topography of the lunar poles from radar interferometry: A survey of cold trap locations. Science 284, 1658–1660. doi:10.1126/science.284.5420.1658.

McEwen, A.S., 1996. A precise lunar photometric function. Lunar Planet. Sci., Houston, Texas, 41. Abstract #841.

Mitrofanov, I.G. et al., 2010a. LEND experiment onboard LRO: Testing local Aaeas with high concentrations of hydrogen at the lunar poles. Lunar Planet. Sci. LXI, The Woodlands, Texas. Abstract #2250.

Mitrofanov, I.G. et al., 2010b. Testing for hydrogen in permanently shadowed regions at the lunar south pole with the lunar exploration neutron detector on board LRO. Science 330, 483–486. doi:10.1126/science.1185696.

Mitrofanov, I.G. et al., 2010c. Lunar exploration neutron detector for the NASA Lunar Reconnaissance Orbiter. Space Sci. Rev. 150, 183–207. doi:10.1007/s11214-009-9608-4.

Noda, H., Araki, H., Goossens, S., Ishihara, Y., Matsumoto, K., Tazawa, S., Kawano, N., Sasaki, S., 2008. Illumination conditions at the lunar polar regions by Kaguya (SELENE) laser altimeter. Geophys. Res. Lett. 35, L24203. doi:10.1029/2008GL035692.

Nozette, S., Lichtenberg, C.L., Spudis, P., Bonner, R., Ort, W., Malaret, E., Robinson, M., Shoemaker, E.M., 1996. The Clementine bistatic radar experiment. Science 274, 1495–1498. doi:10.1126/science.274.5292.1495.

Paige, D.A. et al., 2010. Diviner lunar radiometer observations of cold traps in the Moon's south polar region. Science 330, 479–482. doi:10.1126/science.1187726.

Robinson, M.S. et al., 2010. Lunar Reconnaissance Orbiter Camera (LROC) instrument overview. Space Sci. Rev. 150, 81–124. doi:10.1007/s11214-010-9634-2.

Seidelmann, P.K. et al., 2007. Report of the IAU/IAG working group on cartographic coordinates and rotational elements: 2006. Mech. Dynam. Astron. 98, 155–180.

Shoemaker, E.M., Robinson, M.S., Eliason, E., 1994. The south pole region of the Moon as seen by Clementine. Science 266, 1851–1854.

Smith, D.E., Zuber, M.T., Neumann, G.A., Lemoine, F.G., 1997. Topography of the Moon from the Clementine LIDAR. J. Geophys. Res. 102, 1591–1611.

Smith, D.E. et al., 2010a. The Lunar Orbiter Laser Altimeter investigation on the Lunar Reconnaissance Orbiter mission. Space Sci. Rev. doi:10.1007/s11214-009-9512-.

Smith, D.E. et al., 2010b. Initial observations from the Lunar Orbiter Laser Altimeter. Geophys. Res. Lett 37, L18204. doi:10.1029/2010GL043751.

Stubbs, T.J., Wang, Y., Mazarico, E., Neumann, G.A., Smith, D.E., Zuber, M.T., Torrence, M.H., 2010. Characterizing the optical shadowing at the Moon using LOLA topographic data: Predictions for the LCROSS impact. Lunar Planet. Sci., The Woodlands, Texas, 41. Abstract #2410.

Tooley, C.R., Houghton, M.B., Saylor Jr., R.S., Peddie, C., Everett, D.F., Baker, C.L., Safdie, K.N., 2010. Lunar Reconnaissance Orbiter mission and spacecraft design. Space Sci. Rev. 150, 23–62. doi:10.1007/s11214-009-9624-4.

Vasavada, A.R., Paige, SD.A., Wood, S.E., 1999. Near-surface temperatures on Mercury and the Moon and the stability of polar ice deposits, 1999. Icarus 141, 179–193. doi:10.1006/icar.1999.6175.

Watson, K., Murray, B.C., Brown, H., 1961. The behavior of volatiles on the lunar surface. J. Geophys. Res. 66, 3033–3045.

Williams, J.G., Boggs, D.H., Folkner, W.M., 2008. DE421 Lunar Orbit, Physical Librations, and Surface Coordinates, JPL IOM 335-JW,DB,WF-20080314-001, March 14, 2008.

Zuber, M.T., Garrick-Bethell, I., 2005. What do we need to know to land on the Moon again? Science 310, 983–985.

Zuber, M.T., Smith, D.E., 1997. Topography of the lunar south polar region: Implications for the size and distribution of permanently shaded areas. Geophys. Res. Lett. 24, 2183–2186.

Zuber, M.T., Smith, D.E., Lemoine, F.G., Neumann, G.A., 1994. The shape and internal structure of the Moon from the Clementine mission. Science 266, 1839–1843.